

# High-Wavenumber Finite Differences and Turbulence Simulations

Jason Maron

*Department of Physics, University of Rochester and University of Iowa*

## ABSTRACT

We introduce a fluid dynamics algorithm that performs with nearly spectral accuracy, but uses finite-differences instead of FFTs to compute gradients and thus executes 10 times faster. The finite differencing is not based on a high-order polynomial fit. The polynomial scheme has superb accuracy for low-wavenumber gradients but fails at high wavenumbers. We instead use a scheme tuned to enhance high-wavenumber accuracy at the expense of low wavenumbers, although the loss of low-wavenumber accuracy is negligibly slight. A tuned gradient is capable of capturing all wavenumbers up to 80 percent of the Nyquist limit with an error of no worse than 1 percent. The fact that gradients are based on finite differences enables diverse geometries to be considered and eliminates the parallel communications bottleneck.

## 1. Introduction

The spectral fluid algorithm (Canuto et. al. 1987) uses Fast Fourier Transforms (FFTs) to compute gradients, the most precise means possible. Finite-difference gradients based on a polynomial fit execute faster than FFTs but with less accuracy, necessitating more grid zones to achieve the same resolution as the spectral method. The loss of accuracy outweighs the gain in speed and the spectral method has more resolving power than the finite-difference method. We introduce an alternative finite-difference formula not based on a polynomial fit that executes as quickly but with improved accuracy, yielding greater resolving power than the spectral method.

In section 2 we derive high-wavenumber finite difference formulas and exhibit their effect on the resolving power of a turbulence simulation in section 3. In section 4 we apply finite differences for the purpose of mimicking the spectral algorithm, and then proceed to other applications in section 5.

## 2. Finite differences

Define a function  $f_j(x_j)$  on a set of grid points  $x_j = j$  with  $j$  an integer. Then construct a gradient  $f'(0)$  at  $x = 0$  from sampling a stencil of grid points with radius (or order)  $S$  on each side.

---

<sup>1</sup>maron@tapir.caltech.edu

The familiar result for the gradient on a radius-1 stencil is  $f'(0) \sim (f_1 - f_{-1})/2$ , which is obtained from fitting a polynomial of degree 2 to  $f_j$ . For a degree 4 polynomial on a radius-2 stencil,

$$f'(0) \sim \frac{1}{12}f_{-2} - \frac{2}{3}f_{-1} + \frac{2}{3}f_1 - \frac{1}{12}f_2.$$

For a stencil of order  $S$ ,

$$f'(0) \sim \sum_{j=-S}^S M_j f_j \tag{1}$$

where  $M_{-j} = -M_j$ .

Consider the finite-difference error at  $x=0$  for a Fourier mode  $\sin(\pi kx)$ . Cosine modes can be ignored because they don't contribute to the derivative at  $x = 0$ . Note that the wavenumber  $k$  is scaled to grid units so that  $k = 1$  corresponds to the maximum wavenumber expressible on the grid, also known as the Nyquist limit. The finite difference formula (1) gives  $f'_k(0) \sim 2 \sum_{j=1}^m M_j \sin(jk)$ . Whereas the correct value should be  $k\pi$ , define an error function

$$E_S(k) = k\pi - 2 \sum_{j=1}^S M_j \sin(\pi k j).$$

Figure 1 shows  $E_S(k)$  for stencils of radius 1 through 24. The first order finite difference formula is quite lame, delivering 1 percent accuracy only for  $k$  less than 0.12. Brandenburg (2001) recognized that higher-order finite differences can significantly extend the wavenumber resolution of the polynomial-based finite difference. The 8th order finite difference accuracy is better than 1 percent up to  $k = .56$  and the 16th order finite difference up to  $k = .66$ . Nevertheless these are still far from the Nyquist limit of  $k = 1$  and even higher-order finite-differences yield little further progress.

A Fourier transform gives the correct gradient for all  $k$  up to unity. This is why the spectral algorithm delivers the most resolution per grid element. The resolution limit is set by the maximum  $k$  for which gradients can be captured accurately. Although the 8th order finite-difference formula involves considerably fewer floating point operations than an FFT, the loss of resolution still renders it less efficient than the spectral method.

Polynomial-based finite differences have high accuracy at low  $k$  but fail at large  $k$ . We can instead construct a more practical scheme to improve high- $k$  accuracy at the expense of low- $k$  accuracy, yet the loss of low- $k$  accuracy is negligibly small. From equation 2, we see that the problem of computing accurate gradients reduces to optimizing, or “tuning” the coefficients  $M_j$  to minimize the error over a suitable range of  $k$ , or equivalently to construct a sine series that best mimics a linear function. A set of tuned coefficients appear in table 2 with the associated error functions in figure 1. The error in the radius-8 tuned finite difference is less than 1 percent up to  $k = .80$ , a dramatic improvement over the radius-8 polynomial. An algorithm based on tuned gradients still has a lower maximum  $k$  than the spectral algorithm but due to its increased speed it has greater resolving power (section 3). Henceforth we denote these tuned gradients as “hypergradients.”

### 2.1. Tuning the hypergradient coefficients

Minimizing the error function involves a multiparameter optimization of the coefficients  $M_j$ , - a problem-dependent task with multiple legitimate options. In fact, a high degree of customization is possible for the form of the error function. For this application we proceed as follows. Define a target  $k_{max}$  and an indicator for the quality of the tuned coefficients:

$$E = \int_0^{k_{max}} dk \left[ \pi k - 2 \sum_{j=1}^m M_j \sin(\pi j k) \right]^4 .$$

Then, perform a multi-dimensional optimization on  $M_j$ . The use of a fourth power ensures an approximately uniform error within  $0 < k < k_{max}$ , although a weight function could be added to further customize the form of the error function.  $k_{max}$  is then adjusted until the error is 1 percent. The procedure is repeated for each order  $S$  to yield the coefficients in table 2.

It is worth noting that the radius-8 tuned coefficients are similar to the radius-24 polynomial coefficients. This is not surprising because the polynomial coefficients are too small to matter outside of radius 8.

Stencil radius	1	2	3	4	5	6	8	16	24
Polynomial	.12	.24	.34	.40	.44	.48	.56	.66	.72
Hypergradient	.20	.38	.54	.64	.70	.74	.80	.84	.92

Table 1: Maximum resolved wavenumber  $K$  for the polynomial and hypergradient finite differences shown in figure 1. The tolerance in the relative error is 1 percent.

Operation	$M_0$	$M_1$	$M_2$	$M_3$	$M_4$	$M_5$	$M_6$	$M_7$	$M_8$
$\partial/\partial x$ (T1)	0	.5245							
$\partial/\partial x$ (T2)	0	.73694	-.12780						
$\partial/\partial x$ (T3)	0	.83793	-.23758	.05000					
$\partial/\partial x$ (T4)	0	.89562	-.31797	.11245	-.02850				
$\partial/\partial x$ (T5)	0	.92767	-.36886	.16337	-.06469	.01872			
$\partial/\partial x$ (T6)	0	.94453	-.39729	.19577	-.09322	.03843	-.01194		
$\partial/\partial x$ (T8)	0	.96890	-.44249	.25170	-.15066	.08825	-.04856	.02376	-.01051
$\partial^2/\partial x^2$ (T8)	-3.25820	1.97177	-.47293	.19568	-1.0008	.05565	-.03201	.01821	-.01209
$\partial^4/\partial x^4$ (T6)	16.36332	-12.46631	5.65080	-1.78786	.53027	-.12637	.01729		
Interp. (T8)	0	.63108	-.20002	.10804	-.06614	.04104	-.02501	.01406	-.00815
$\partial/\partial x$ (P1)	0	.50000							
$\partial/\partial x$ (P2)	0	.66667	-.08333						
$\partial/\partial x$ (P3)	0	.75000	-.15000	.01667					
$\partial/\partial x$ (P4)	0	.80000	-.20000	.03810	-.00357				
$\partial/\partial x$ (P8)	0	.88889	-.31111	.11313	-.03535	.00870	-.00155	.00018	-.00001

Table 2: The finite-difference coefficients  $M_j$ . The label “ $P(S)$ ” corresponds to the polynomial-based finite difference on a radius  $S$  stencil. “ $T(S)$ ” denotes the tuned hypergradient finite difference coefficients engineered to have a relative error of 1 percent. The entry labeled “Interp” is for the tuned coefficients used in interpolating halfway between two grid points. The entry labeled “Padé” gives the coefficients for the Padé derivative in explicit finite-difference form.

Operation	$M_0$	$M_1$	$M_2$	$M_3$	$M_4$	$M_5$	$M_6$	$M_7$	$M_8$
$\partial/\partial x$ (T16)	0	.98043	-.46188	.27843	-.18085	.11956	-.78175	.49510	-.29766
Interp. (T16)	0	.63395	-.20433	.11458	-.07387	.05001	-.03428	.02333	-.01555
$\partial/\partial x$ (P16)	0	.94118	-.39216	.19264	-.09391	.04293	-.01789	.00667	-.00219
$\partial/\partial x$ (P24)	0	.96000	-.42462	.23066	-.12974	.07158	-.03778	.01880	-.00874
$\partial/\partial x$ (FFT)	0	1.0000	-.50000	.33333	-.25000	.20000	-.16667	.14286	-.12500
$\partial/\partial x$ (Padé)	0	.87910	-.35546	.13577	-.05186	.01981	-.00757	.00289	-.00110
Operation	$M_9$	$M_{10}$	$M_{11}$	$M_{12}$	$M_{13}$	$M_{14}$	$M_{15}$	$M_{16}$	
$\partial/\partial x$ (T16)	.16517	-.80806	.30987	-.48958	-.65096	.86017	-.69157	.44690	
Interp. (T16)	.01005	-.00622	.00365	-.00199	.00099	-.00043	.00015	-.00002	
$\partial/\partial x$ (P16)	.00062	-.00015	.00003	$\sim 0$	$\sim 0$	$\sim 0$	$\sim 0$	$\sim 0$	
$\partial/\partial x$ (P24)	.00377	-.00150	.00054	-.00018	.00005	-.00001	$\sim 0$	$\sim 0$	
$\partial/\partial x$ (FFT)	.11111	-.10000	.09091	-.08333	.07692	-.07143	.06667	-.06250	
$\partial/\partial x$ (Padé)	.00042	-.00016	.00006	-.00002	.00001	$\sim 0$	$\sim 0$	$\sim 0$	

Table 3: Finite-difference coefficients for large stencil radii, with the same notation as for table 2. The label “FFT” denotes the coefficients for a Fourier transform (section 2.2).

## 2.2. Compactness

The Padé scheme evaluates implicit derivatives:

$$f'_i + \sum_{j=1}^{p'} P'_j (f'_{i+j} + f'_{i-j}) = \sum_{j=1}^p P_j (f_{i+j} - f_{i-j}) \quad (2)$$

The case  $p' = 1$  involves a cyclic tridiagonal matrix,  $p' = 2$  a cyclic pentadiagonal matrix, etc. The Padé scheme is not compact because the gradient evaluation draws information from all grid points, propagated around the grid by the cyclic matrix. The contribution from each grid point can be explicitly evaluated from the matrix inverse to express it in the form of equation 1. The 6th order tridiagonal scheme with  $P'_1 = 1/3$ ,  $P_1 = 7/9$ ,  $P_2 = 1/36$  yields the coefficients denoted “Padé” in table 3, where the entries  $M_j$  have significant magnitudes up to  $j = 6$ , in spite of the fact that  $P_j$  extends only to  $j = 2$ . The Padé scheme has a maximum wavenumber of  $K = .50$  whereas the radius-6 tuned scheme has  $K = .74$ . The tuned scheme is maximally compact in the sense that it

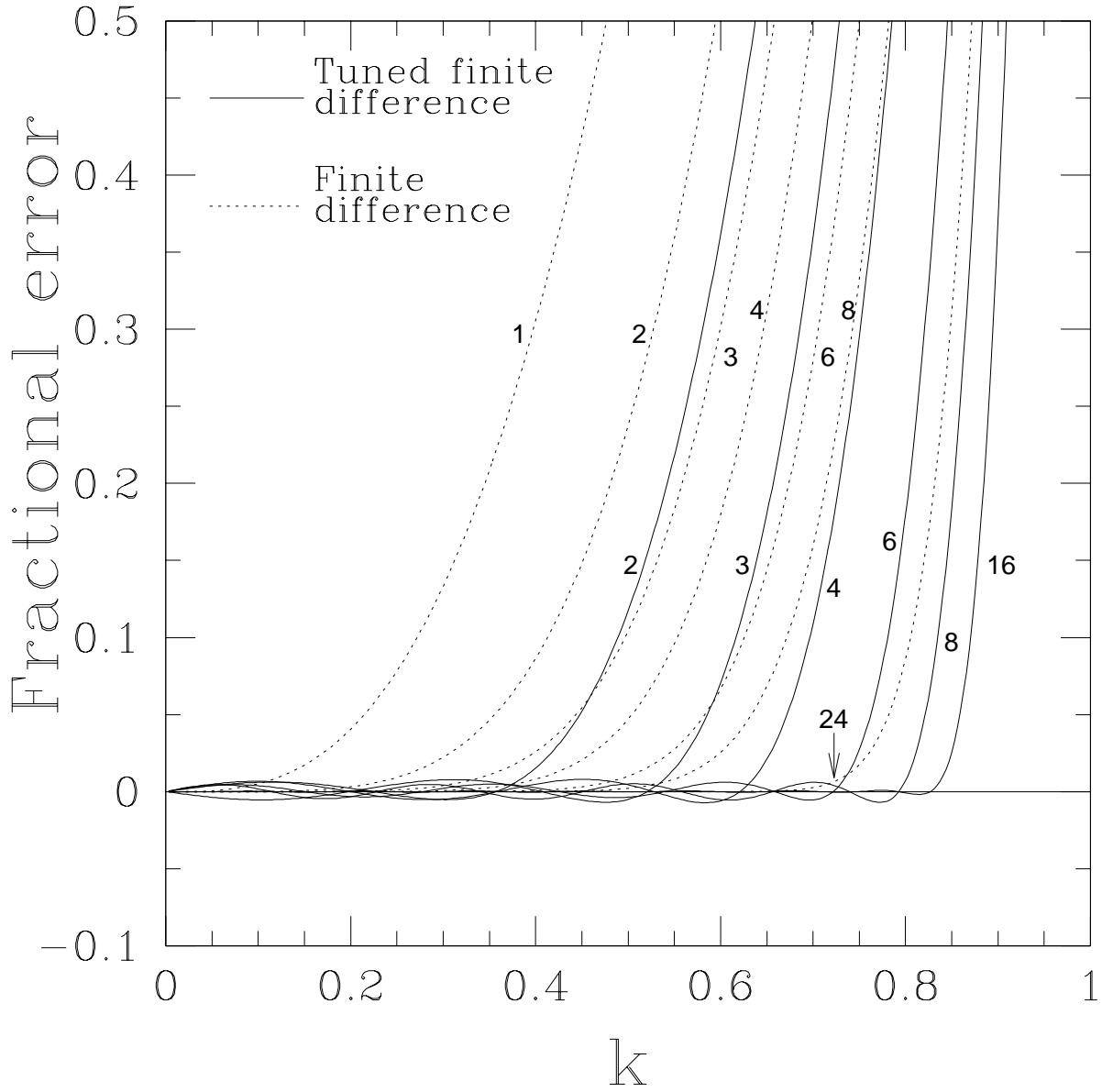


Fig. 1.— *Figure 1: The relative gradient error for the polynomial-based finite difference (dotted line) and tuned finite difference (solid line). Numbers indicate the stencil radius.*

has the best wavenumber-accuracy properties if the information to be drawn from is confined to within a given stencil radius.

The spectral gradient is particularly noncompact. The coefficients for a size  $N$  transform expressed in the form of equation 1 are

$$M_j = \frac{4\pi}{N^2} \sum_{s=1}^{N/2} s \sin(2\pi s j / N) \quad \longrightarrow \quad j^{-1} \quad (N \rightarrow \infty). \quad (3)$$

It is interesting to note that these are the coefficients for the linear function expressed as an infinite sine series. Unfortunately, quite a few terms are needed before the series starts to resemble the linear function.

### 2.3. Higher-order gradients and other operations

Diffusion involves second-order gradients. For these, we utilize the cosine modes to construct an error function analogous to equation (2):

$$E_S^{(2)}(k) = (k\pi)^2 + M_0 + 2 \sum_{j=1}^S M_j \cos(\pi k j).$$

For fourth-order gradients,

$$E_S^{(4)}(k) = -(k\pi)^4 + M_0 + 2 \sum_{j=1}^S M_j \cos(\pi k j).$$

A low pass filter can mimic a high-order hyperdiffusivity. To construct this, replace the  $(\pi k)^2$  term with something that is zero at low  $k$  and large at high  $k$  with a sharp transition at the desired cutoff  $k$ .

An interpolation halfway between two grid points is useful for resolution refinement and dealiasing:

$$E_S^{(I)}(k) = -\pi + 2 \sum_{j=1}^S M_j \cos(\pi k (j - 1/2)). \quad (4)$$

Here,  $j = 1$  corresponds to the nearest point,  $j = 2$  to the next most distant point, etc.

## 3. Resolving power of a turbulence simulation

We address two elements of computational efficiency - execution speed and resolution per grid element, which together constitute the resolving power. Other factors exist that won't be considered here, such as Lagrangian vs. Eulerian timesteps, and variable timesteps.

Define the execution speed as the number of grid zones (or particles, for an SPH code) processed per CPU GigaFlop per second, or Kilo-Elements per GFlop per second (Kegs). Also define a resolution per grid element ( $K$ ) as a measure of the effective resolution of a grid element or particle:

$$K = \frac{k_{Max}}{k_{Nyquist}}$$

where  $k_{Max}$  is the maximum wavenumber for which accurate gradients can be computed and  $k_{Nyquist}$  is the Nyquist wavenumber, the maximum wavenumber expressible on the grid.  $k_{Nyquist} = \pi/\Delta$  for a grid spacing of  $\Delta$ . The value of  $K$  for various finite difference schemes appears in table 1.

The resolving power (R) is the measure of the speed of a code at a fixed benchmark resolution. For example, a code with high  $K$  requires fewer grid cells and hence executes faster than a code with lower  $K$ . The scaling for a 3D algorithm based on explicit time differences of second-or-higher order is

$$R = [\text{Kegs}] \cdot K^3.$$

For a flux-transport algorithm, it is  $R = [\text{Kegs}] \cdot K^4$ .

Many algorithms such as the Riemann shock solver aren't based on explicit gradients and lack an easily definable  $K$ .  $K$  can alternatively be defined in terms of the maximum achievable Reynolds number  $R_e$  on an  $N^3$  grid:  $R_e = (ANK)^{4/3}$ . Maron & Cowley (2001) found that a  $128^3$  spectral simulation with a  $K = 2/3$  dealiasing truncation had  $R_e = 2500$  implying  $A \sim 4.1$ . For algorithms with intrinsic numerical viscosity plus an explicit Laplacian viscosity, the value of the viscosity parameter can be varied to identify the minimum meaningful viscosity and from that an effective Reynolds number follows.

### 3.1. Transforms

A 3D spectral code is based on real-to-complex and complex-to-real Fast Fourier Transforms (FFTs) on an  $N^3$  grid. This transform requires  $7.5 \log_2(N)$  floating point operations per grid point. The FFT is difficult to optimize and executes at only some fraction of the peak floating point speed. For the purposes of wallclock execution time, we may think of the FFT as having effectively  $7.5 \log_2(N)/f_{FFT}$  operations per grid point where  $f_{FFT}$  is the efficiency factor associated with algorithm. We further identify separate efficiency factors for the serial and parallel aspects of the algorithm by  $F_{FFT}^s$  and  $F_{FFT}^p$  respectively. The FFT poses a challenge to optimization because the 1D stage of the transform involves highly irregular memory access (and hence memory latency), the 3D stage requires non-consecutive array access over the slow indices, and the parallel stage requires communication between every processor pair. Frigo and Johnson (1998) met this challenge in grand style with their cross-platform application ‘‘Fastest Fourier Transform in the West (FFTW),’’ which is usually the best performer on any given architecture. On the Pittsburgh Supercomputing Center’s Alpha ES45 ‘‘Lemieux’’ it does especially well, with  $f_{FFT}^s = 0.32$  and  $f_{FFT}^p = 0.38$  for a  $1024^3$

transform on 512 processors. For a  $512^3$  grid on 256 processors,  $f_{FFT}^s = 0.32$  and  $f_{FFT}^p = 0.44$ . Other large-grid, large-CPU transforms perform similarly (figure 2). We take these parameters as the practical limit of FFT efficiency.

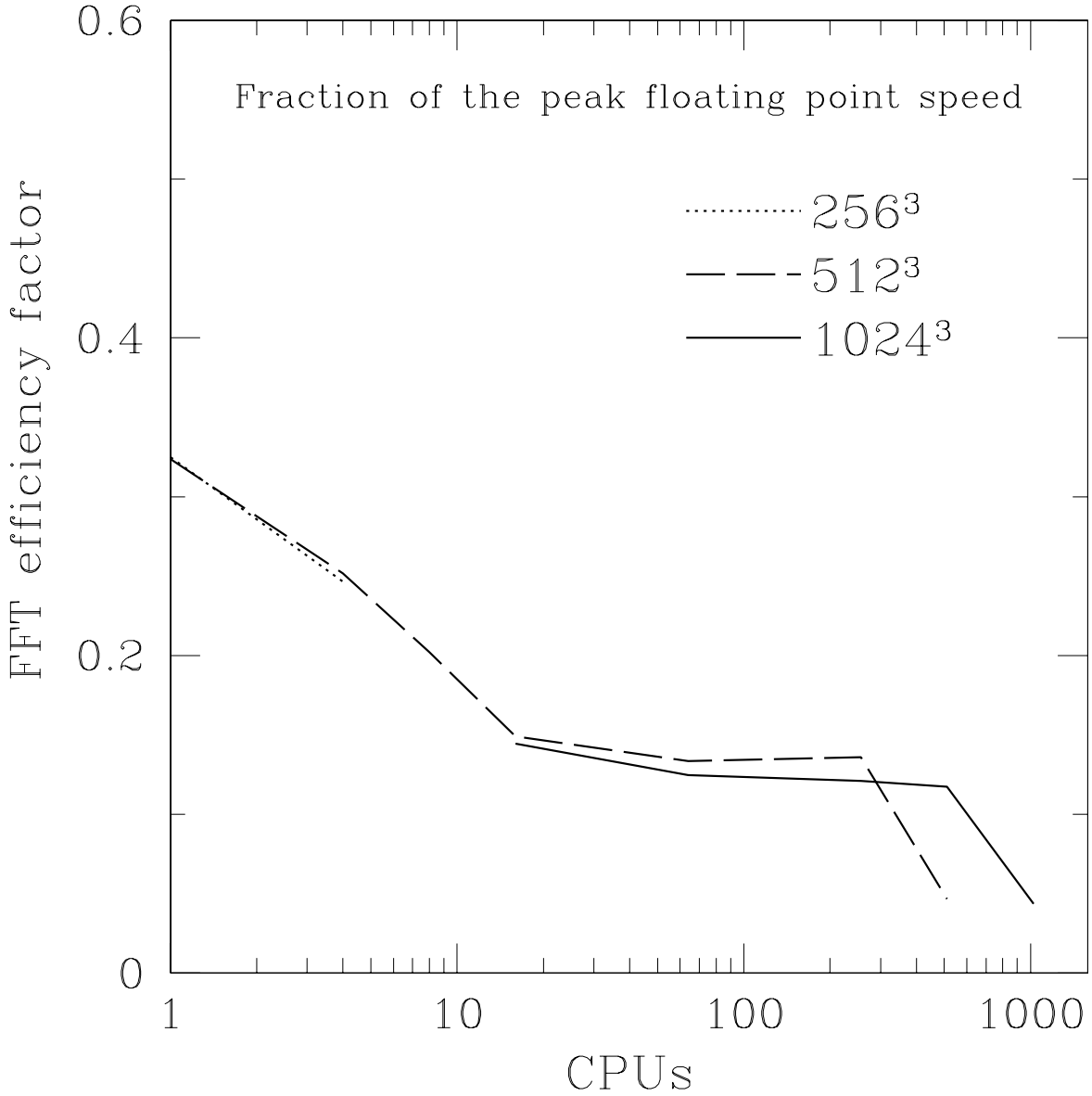


Fig. 2.— *Figure 2: The performance of FFTW for  $256^3$ ,  $512^3$ , and  $1024^3$  transforms on the Pittsburgh Supercomputing Center’s MPI-parallel machine “Lemieux.” The efficiency factor is the fraction of the peak floating point speed. Note that the parallel inefficiency takes effect at a low number of CPUs and plateaus at a high number of CPUs.*



### 3.2. The finite-difference gradient transform

The finite-difference gradient transform (equation 1) on a radius  $S$  stencil has a floating point operation count per grid element of  $(4S - 2)$ . Unlike the FFT, memory access is linear and parallel communication occurs only between the two adjacent processors. The transform can be optimized so that the serial and parallel efficiency factors  $f_{FD}^s$  and  $f_{FD}^p$  are much closer to unity than for the FFT case. On the Pittsburgh Supercomputing Center’s Alpha ES45 “Lemieux”,  $f_{FD}^s = 0.85$  and  $f_{FD}^p = 0.8$  to yield an overall finite-difference efficiency factor of  $f_{FD} = 0.68$ .

### 3.3. Padé gradients

The Padé scheme is nonlocal - the transform has to be computed simultaneously on a 1D cut that transverses the volume. The operation count is 5 adds and multiplies plus one divide for the tridiagonal scheme, and 7 adds and multiplies plus one divide for the pentadiagonal scheme (Lele 1992). On the HP ES45, a divide takes 12 clocks, and since it can’t be pipelined the effective cost is 24 floating point operations. This is because ordinarily the ES45 produces one add and one multiply result per clock cycle. The total number of floating point operations is then  $34/f_{Pade}$  for the tridiagonal scheme and  $38/f_{Pade}$  for the pentadiagonal scheme, where  $f_{Pade}$  is the efficiency factor of the algorithm.

The fact that the Padé scheme is nonlocal eliminates the possibility of adaptive resolution through a variable stencil size, and also degrades the performance at boundaries. The fact that it’s a matrix operation makes it more difficult to pipeline efficiently whereas the tuned finite-difference gradient is a straightforward local convolution. The locality of the tuned gradient involves communication only between adjacent processors whereas the Padé method is nonlocal and requires an all-to-all communications stage. This seriously degrades the Padé scheme’s parallel scalability, especially for large numbers of CPUs (section 3.7).

### 3.4. Operation count for one timestep

The floating point operation count per timestep is the operation count per transform times the number of transforms. For the transform count, assume a Runge-Kutta 2nd order timestep (RK2) so that the field gradients are evaluated twice per timestep. A spectral hydro simulation involves 3 transforms from Fourier to real space and 6 transforms back to Fourier space, all done twice for a total of 18 transforms. The MHD case has 30 transforms.

Aliasing error limits the spectral resolution of a bilinear partial differential equation to  $K = 2/3$ , or  $K = \sqrt{8/9} = .94$  with the inclusion of a phase shift correction (Canuto et. al. 1987). The correction is implemented by calculating the time derivatives on two grids - the original grid and a grid shifted to the zone center - and averaging the results after shifting back to the original

grid. The procedure can be coordinated with the Runge-Kutta algorithm by calculating the two Runge-Kutta stages on grids shifted diagonally from each other by half a grid zone (Canuto et. al. 1987). The grid shift adds negligible extra computation for the spectral algorithm because it can be carried out in Fourier space as a mere multiply. For a finite-difference code it costs two real-space interpolations per dynamical field. The interpolation can be tuned for enhanced wavenumber accuracy analogously with finite-difference gradients. The radius-4 hypergradient is accurate up to  $K = .64$  and needs no grid-shift aliasing correction whereas higher-order hypergradients do.

To estimate the operation count of the finite-difference method we assume the adiabatic equations of MHD, although other forms are possible.

$$\partial_t \mathbf{V} = -\mathbf{V} \cdot \nabla \mathbf{V} - \rho^{-1} \nabla P + \rho^{-1} (\nabla \times \mathbf{B}) \times \mathbf{B} + \nu \nabla^2 \mathbf{V} + \nu_4 \nabla^4 \mathbf{V} \quad (5)$$

$$\partial_t \mathbf{B} = -\nabla \times (\mathbf{V} \times \mathbf{B}) + \eta \nabla^2 \mathbf{B} + \eta_4 \nabla^4 \mathbf{B} \quad (6)$$

$$\partial_t \rho = -\nabla \cdot (\rho \mathbf{V}) \quad P \sim \rho^\gamma \quad \nabla \cdot \mathbf{B} = 0 \quad (7)$$

$\mathbf{V}$	Velocity field	$\mathbf{B}$	Magnetic field
$\nu$	Viscosity	$\eta$	Magnetic resistivity
$\nu_4$	4th order hyperviscosity	$\eta_4$	4th order magnetic hyperresistivity
$P$	Fluid Pressure	$\rho$	Density
$\gamma$	Adiabatic index		

For hydrodynamics (without a magnetic field) there are 9 velocity and 3 density gradients. A magnetic field adds 9 magnetic gradients. Diffusion terms don't add to the computation because they only need to be applied once every few timesteps (section 3.5). Each gradient is evaluated twice per timestep for Runge-Kutta order 2. The grid shifts are evaluated twice per field per timestep for stencil radii larger than 4. These considerations determine the number of transforms in table 4. Note that for the finite difference and Padé cases, each coordinate direction is counted as one transform. For the FFT case, the 3D transform is counted as one transform.

Algorithm	Physics	Stencil radius (S)	Ops/ element transform	Trans- forms	Speed (Kegs)	Max wave- number (K)	Resolving Power (Kegs · K <sup>3</sup> )
Hypergradient	Hydro	2	$6f_{FD}^{-1}$	24	$6940f_{FD}$	.38	$381f_{FD}$
Hypergradient	Hydro	3	$10f_{FD}^{-1}$	24	$4170f_{FD}$	.54	$656f_{FD}$
Hypergradient	Hydro	4	$14f_{FD}^{-1}$	24	$2980f_{FD}$	.64	$780f_{FD}$
Hypergradient	Hydro	8	$30f_{FD}^{-1}$	32	$1040f_{FD}$	.80	$533f_{FD}$
Hypergradient	Hydro	16	$62f_{FD}^{-1}$	32	$504f_{FD}$	.84	$299f_{FD}$
Hypergradient	MHD	2	$6f_{FD}^{-1}$	42	$3970f_{FD}$	.38	$218f_{FD}$
Hypergradient	MHD	3	$10f_{FD}^{-1}$	42	$2380f_{FD}$	.54	$375f_{FD}$
Hypergradient	MHD	4	$14f_{FD}^{-1}$	42	$1700f_{FD}$	.64	$446f_{FD}$
Hypergradient	MHD	8	$30f_{FD}^{-1}$	56	$595f_{FD}$	.80	$305f_{FD}$
Hypergradient	MHD	16	$62f_{FD}^{-1}$	56	$288f_{FD}$	.84	$171f_{FD}$
Spectral	Hydro	N/2	625	18	89	.94	74
Spectral	MHD	N/2	625	30	53	.94	44
Polynomial	Hydro	1	$2f_{FD}^{-1}$	24	$20833f_{FD}$	.12	$36f_{FD}$
Polynomial	Hydro	2	$6f_{FD}^{-1}$	24	$6940f_{FD}$	.24	$96f_{FD}$
Polynomial	Hydro	3	$10f_{FD}^{-1}$	24	$4170f_{FD}$	.34	$164f_{FD}$
Polynomial	Hydro	4	$14f_{FD}^{-1}$	24	$2980f_{FD}$	.40	$190f_{FD}$
Polynomial	Hydro	6	$22f_{FD}^{-1}$	24	$1890f_{FD}$	.48	$209f_{FD}$
Padé tridiag.	Hydro	N/2	$34f_{\text{Pade}}^{-1}$	24	$1230f_{\text{Pade}}$	.50	$153f_{\text{Pade}}$
Padé pentadiag.	Hydro	N/2	$38f_{\text{Pade}}^{-1}$	32	$822f_{\text{Pade}}$	.83	$470f_{\text{Pade}}$
Padé tridiag.	MHD	N/2	$34f_{\text{Pade}}^{-1}$	42	$700f_{\text{Pade}}$	.50	$88f_{\text{Pade}}$
Padé pentadiag.	MHD	N/2	$38f_{\text{Pade}}^{-1}$	56	$470f_{\text{Pade}}$	.83	$269f_{\text{Pade}}$

Table 4: The speed, resolution, and resolving power for spectral and finite-difference algorithms. The value of  $K = .94$  for the spectral algorithm arises from the  $\sqrt{8/9}$  rule for the 3D staggered-grid dealiasing procedure (Canuto et. al. 1987). Execution speed is estimated from the transform time while other overhead is ignored. The finite-difference efficiency factor is approximately  $f_{FD} \sim .7$

Assuming that the finite-difference efficiency factor  $f_{FD} = f_s f_p$  can be optimized to a better degree than for the FFT transform, the tuned gradient method could potentially be up to 7 times faster than the spectral method. The most efficient hypergradient configuration is with a stencil radius of 4 because larger stencil radii require an aliasing correction. More resolution could be achieved with a loss of efficiency by using larger-radius stencils.

### 3.5. Diffusion

Diffusion serves two roles: the removal of energy cascading to the inner scale, and as a dealiasing filter. If diffusion is the only agent acting in the Navier-Stokes equation, the Fourier component  $\hat{\mathbf{V}}$

evolves as  $\partial_t \hat{\mathbf{V}} = -\nu k^2 \hat{\mathbf{V}}$ . Defining  $k_<$  to be the limiting resolution, the inner-scale modes evolve with a timescale of  $t_< \sim 1/(\nu k_<^2)$ . The diffusion  $\nu$  is generally set so that  $t_<$  corresponds to the dynamical cascade timescale so that diffusion balances energy cascading to the inner scale. This is also known as the Lagrangian timescale. The timestep, however, is proportional to the Eulerian timescale, the time for the fluid to flow a distance equal to the resolution scale. Generally, the Lagrangian timescale greatly exceeds the Eulerian timescale and so diffusion has only a small effect each timestep. We can therefore economize by applying kinetic and magnetic diffusion only once every few timesteps with a corresponding increase in the values of  $\nu$  and  $\eta$ . This effectively removes diffusion from the computational load. In section 4 we find that once every four timesteps yields equivalent results as once every timestep. Furthermore, the coefficients of the second and fourth order diffusion operators as well as those for a dealiasing filter can be added to compactify them into one operator.

### 3.6. Magnetic divergence

Magnetic divergence can be suppressed either with a scheme that preserves it exactly, such as the constrained-transport algorithm (Stone & Norman, 1992 I, 1992 II), or by letting it evolve unconstrained and periodically repairing it such as with an FFT. The constrained-transport scheme derives electric field interpolations and gradients from first first-order finite differences and hence has poor wavenumber resolution. High-wavenumber finite differences improve this situation and in fact magnetic divergence grows slowly enough so as to not be concern (section 4.)

### 3.7. Parallelization

Good parallel scalability occurs if the demand for communications is less than that for floating point arithmetic so that both can occur simultaneously, otherwise communications hinder execution. The relevant indicator is the ratio  $R$  of floating point operations per second divided by the transmission rate of floating point variables between processors. For a machine such as the Pittsburgh Supercomputing Center’s 3000 processor HP Alpha ES45 “Lemieux,” the ratio is  $R_{Arch} = 2 \text{ GFlops} / (68 \cdot 10^6 \text{ reals/s}) \sim 30$  (San Diego Supercomputing Center study, 2003). CPU technology tends to improve more rapidly than communications and so this ratio may increase over the next few years (table 5).

A finite-difference transform on a radius  $S$  stencil invokes  $2S - 1$  adds and  $S$  multiplies, effectively totaling  $4S - 2$  operations since add and multiply units appear in pairs. Summed over the three coordinate directions this is  $12S - 6$  floating point operations. For parallel execution, let the data be distributed in slabs of dimension  $(N, N, N')$  where the grid size is  $N^3$  and the number of CPUs is  $C = N/N'$ . To compute the  $z$  gradient transform every processor summons and sends  $2N^2S$  reals to and from adjacent processors. The two-way MPI pass proceeds at double the

one-way rate quoted in table 3.9. The ratio of floating point operations to passed variables is then  $R_{FD} = N'(6 - 3/S)$ . Efficient parallel scalability can occur if  $R_{FD} > R_{Arch}$  or  $N' > 4$ .

For the Padé transform, the entire 1D coordinate slice has to be on the same processor. For slab geometry, the  $x$  and  $y$  transforms can be done with the data on hand and then a global interprocessor transpose reorganizes the data along  $z$  for the  $z$  transform. A final transpose returns to the original slab to calculate the time derivatives. The ratio of floating point operations to passed variables is  $R_{Pade} = 3F/2$  where  $F$  is the number of floating point operations per grid element in the 1D transform. With  $F = 34$  for the radius-2 tridiagonal configuration and  $F = 38$  for the radius-3 pentadiagonal configuration (table 4) it's at the threshold of efficient parallelizability.

The spectral method consists of 1D  $x$ ,  $y$  and  $z$  transforms to convert from Fourier space to real space and back. Only one transpose per  $z$  transform is necessary because the real-space products can be conducted in the transposed state. Therefore the ratio of floating point operations to passed variables is  $R_{FFT} = 75/f_s$  where  $f_{FFT}^s \sim .32$  is the efficiency factor for the serial stage of the computation (section 3.1). In spite of the fact that  $R_{FFT}$  is approximately 8 times  $R_{Arch}$  for the supercomputer “Lemieux”, the parallel efficiency is only  $f_{FFT}^p = .38$ , implying that the all-to-all transpose is substantially slower than the peak transmission rate would suggest. Since the Padé transform has about 10 times fewer floating point operations than the spectral transform, it is likely that the Padé scheme would be seriously inefficient in parallel execution. Since the finite-difference transform only involves passing between the adjacent CPUs, it does not suffer from this problem.

### 3.8. Memory

A code based on tuned finite differences can calculate the entire time update for small sections of the simulation volume at a time, eliminating the need for large temporary storage so that only the dynamical fields  $\{\mathbf{V}, \mathbf{B}, \rho\}$  count toward the memory requirement. This is 7 arrays of size  $(N, N, N')$  where  $N'$  is  $N$  divided by the number of CPUs. It is safe to assume that the temporary storage plus the memory taken by the operating system will exceed the size of one array. Given that computer memory tends to come in powers of 2, we assume that the total memory requirement per CPU is equal to the size of 16 arrays of 4 Byte reals. Table 6 shows how grids less than or equal to  $1024^3$  can be fit easily onto most supercomputers and a  $2048^3$  grid could fit onto a supercomputer with 512 CPUs and 1 GB/CPU.  $N'$  should be at least 4 for good parallel scalability (section 3.7), and so  $2048^3$  simulations are feasible on most existing supercomputers (table 5).

A code based on Padé gradients cannot be arranged to compute the time update for subsections successively as could be done for tuned finite differences. This is because the Padé transform is nonlocal whereas the tuned finite difference operates on a local stencil only. Hence, the entire grid has to be updated all at once, demanding temporary storage for each partial derivative and expanding the memory requirement beyond 16 arrays per CPU. This is also true for a spectral code.

### 3.9. Supercomputers

Machine	Name	Clock (GHz)	GFlops	RAM (GB)	CPUs	MPI speed (GB/s)	Pipe stages	L1 (kB)	L2 (MB)	L3 (MB)	RAM speed (GB/s)
NCSA Xeon	Tungsten	3.1	6.2	1.5	2560	.5			0.5		
ORNL Cray X1	Phoenix	0.8	12.8	4.0	512	5		16	2.0		200
PSC HP ES45	Lemieux	1.0	2.0	1.0	3016	.25	4	64	8.0		5.2
ORNL IBM Power4	Cheetah	1.3	5.2	1.0	864	.25	6	32	1.5	32	200
UIUC Intel Itanium	Titan	0.8	3.2	2.0	256	.1					
UIUC Intel Pentium	Platinum	1.0	1.0	1.5	968	.01	5				
Japan NEC	Earth Sim.	0.5	8.0	2.0	5120						
Iowa Athlon	Zephyr	1.5	1.0	1.0	32	.25	4				
Athlon Opteron		1.6	3.2	1.0				64	1		5.3
SGI Altrix		1.3	2.6					32	.25	3	6.4

Table 5: Academic supercomputers. For Cheetah, some CPUs have 4 GB/CPU but most have 1. The French Alpha ES45 “Ixia” and “Nympea” have the same characteristics as Lemieux. Most of these numbers are from Dunigan 2003. The two-way MPI passing speed is double the tabulated one-way speed. Some entries are missing because this kind of information is often hard to come by on the web.

11 12 13

Grid	CPUs	Memory/CPU (GB)
512 <sup>3</sup>	64	1/8
512 <sup>3</sup>	128	1/16
1024 <sup>3</sup>	128	1/2
1024 <sup>3</sup>	256	1/4
2048 <sup>3</sup>	128	4
2048 <sup>3</sup>	256	2
2048 <sup>3</sup>	512	1

Table 6: Parallel configurations and memory requirements for a finite-difference code.

### 4. Imitating an incompressible spectral MHD code

It is possible to mimic the function of an incompressible spectral code with high-wavenumber finite differences, and with significantly more resolving power (table 4). The principal advantage of

simulating incompressible turbulence is that the sound speed does not impact the Courant timestep condition. We start with the equations of MHD (equations 5 through 7) but with  $\rho$  set to unity and the pressure term deleted. In its place we add terms of the form  $\nu_D \nabla(\nabla \cdot \mathbf{V})$  and  $\eta_D \nabla(\nabla \cdot \mathbf{B})$  to the fluid and magnetic equations respectively to suppress the growth of divergence in the velocity and magnetic fields.  $\nu_D$  and  $\eta_D$  are artificial divergence diffusivities that will be discussed in section 4.1.

#### 4.1. Divergence correction

An artificial term of the form  $\partial_t \mathbf{V} = \nu_D \nabla \nabla \cdot \mathbf{V}$  in the Navier Stokes equation removes divergence while preserving the solenoidal component. Define  $\hat{\mathbf{V}}_{\parallel} = \mathbf{k} \cdot \hat{\mathbf{V}}/k$  and  $\hat{\mathbf{V}}_{\perp} = \hat{\mathbf{V}} - \hat{\mathbf{V}}_{\parallel}$ , and then the artificial term has the effect of  $\partial_t \hat{\mathbf{V}}_{\parallel} = -\nu_D k^2 \hat{\mathbf{V}}_{\parallel}$  and  $\partial_t \hat{\mathbf{V}}_{\perp} = 0$ . It's not surprising that the procedure is most effective for large  $k$  modes. Fully removing the divergence for all modes requires a global operation such as can be accomplished with an FFT. This procedure is instead based on locally calculated gradients.  $\nu_D$  is set so that the divergence in the largest  $k$  modes is completely eliminated in one timestep:

$$\nu_D = \frac{1}{k_{Nyquist} \Delta t} = \frac{1}{\pi^2 N^2 \Delta t},$$

where  $N$  is the number of grid points in each dimension and  $k_{Nyquist}$  is the Nyquist wavenumber. A larger value overcompensates for the largest  $k$  modes. This procedure serves to suppress the growth of divergence for several timesteps, but not indefinitely. Ultimately a complete correction involving FFTs must be applied, especially for low  $k$  modes. Figure 3 shows that divergence can be held to less than 1 percent of the maximum by applying the FFT divergence corrector once every 8 timesteps. At this frequency, the FFT contributes negligibly to the computational load.

Define an energy spectrum:  $\langle V^2 \rangle / 2 = \int E_V(k) dk$ , where  $E_V(k) = 2\pi k^2 \langle |\hat{V}(k)|^2 \rangle$ . Also define a divergence spectrum  $D_V(k) = 2\pi k^2 \langle |\mathbf{k} \cdot \hat{\mathbf{V}}(k)|^2 \rangle$  and a divergence normalization spectrum  $\overline{D}_V(k) = 2\pi k^2 \langle k^2 |\hat{V}(k)|^2 \rangle$ . The divergence normalization serves to define a fractional divergence  $D_V(k)/\overline{D}_V(k)$ . Analogously define a magnetic spectrum  $E_B(k)$ , a magnetic divergence spectrum  $D_B(k)$ , and a magnetic divergence normalization spectrum  $\overline{D}_B(k)$ .

#### 4.2. Diffusivity

Neither the diffusivity operator nor the spectral divergence correction need to occur every timestep (section 3.5). Nearly equivalent evolution results from applying them only once every few timesteps, lessening their impact on the computational load. Let the diffusivity be applied once every  $I_{diff}$  timesteps with  $\nu$  and  $\eta$  replaced by  $\nu I_{diff}$  and  $\eta I_{diff}$ , with similar replacements for the higher order diffusivities. Also, let the spectral divergence correction be applied once every  $I_{FFT}$  timesteps.

### 4.3. Simulations

With the need to study both kinetic and magnetic divergence, we ran tests with fully turbulent kinetic and magnetic fields. Initial conditions come from the magnetic dynamo simulations of Maron & Cowley (2001). There, forced isotropic turbulence with a magnetic field is evolved to its long-term saturated state where the magnetic energy equals the kinetic energy. This is the magnetic analogue to the Kolmogorov cascade. We restarted this simulation without forcing to study the divergence growth rate. Table 7 lists the simulations that were run for this study. Z677 is a high-resolution spectral simulation that serves as a benchmark for comparison. This simulation was run with the spectral code “Tulku” (Maron & Goldreich 2001).

Simulations Z749 through Z754 (table 7) were run to optimize the values of the divergence diffusion parameters  $\nu_D$  and  $\eta_D$ . No spectral divergence correction was applied ( $I_{FFT} = \infty$ ), leaving the divergence suppression solely to  $\nu_D$  and  $\eta_D$ . The initial divergence spectrum is identically zero. The divergence spectrum after 4 timesteps is plotted in figure 3. Increasing  $\nu_D$  and  $\eta_D$  decreases the divergence spectrum until  $\nu_D = \eta_D = .016$ , whereupon further increase results in an overshoot in the correction at large  $k$ . Taking the value of 0.016 as optimal, we plot the growth of the divergence spectrum with this value (simulation Z753) in figure 3. After 4 timesteps, the ratio of the divergence to the divergence normalization spectrum is at most 0.015 for  $\mathbf{V}$  and  $10^{-5}$  for  $\mathbf{B}$ .

In figure 5 we plot the evolution of the finite difference simulation Z748 together with the benchmark spectral simulation Z677, both starting from the same initial conditions. After 0.5

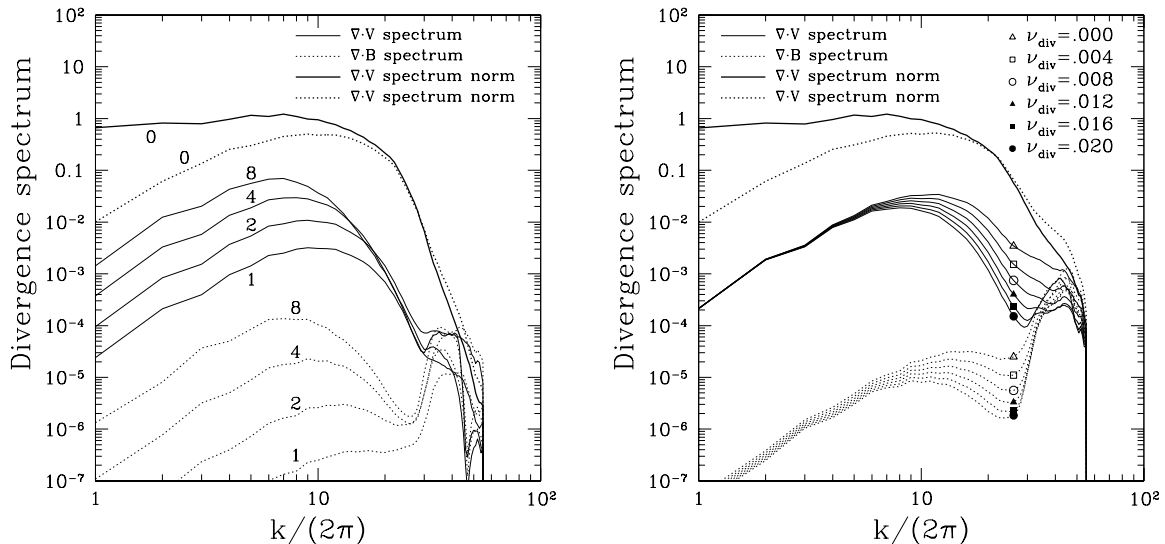


Fig. 3.— *Figure 3: Left: The V and B divergence spectra for simulation Z753. Numbers indicate timesteps. Right: The divergence spectra for simulations Z749 through Z754 after four timesteps of evolution, for a sequence of parameters  $\nu_D$  and  $\eta_D$ .*



dynamical times, the spectra (figure 5) and real space fields (figure 4) are in good agreement. The spectrum for simulation Z748 is slightly diminished from Z677 because the divergence takes with it a small measure of energy. Simulation Z748 has  $I_\nu = I_\eta = 4$  and  $I_{FFT} = 4$ . Another simulation (Z757) has  $I_\nu = I_\eta = 1$  and  $I_{FFT} = 4$  and has exactly the same energy spectrum as Z748, establishing that the diffusion operator doesn't have to be applied every timestep.

Simulation	Grid	Algorithm	$\nu_D$	$\eta_D$	$I_\nu$	$I_\eta$	$I_{FFT}$
Z677	Spectral	$128^3$	0	0	1	1	1
Z745	Hypergradient	$64^3$	.016	.016	1	1	1
Z746	Hypergradient	$64^3$	.016	.016	2	2	2
Z747	Hypergradient	$64^3$	.016	.016	3	3	3
Z748	Hypergradient	$64^3$	.016	.016	4	4	4
Z749	Hypergradient	$64^3$	.000	.000	4	4	$\infty$
Z750	Hypergradient	$64^3$	.004	.004	4	4	$\infty$
Z751	Hypergradient	$64^3$	.008	.008	4	4	$\infty$
Z752	Hypergradient	$64^3$	.012	.012	4	4	$\infty$
Z753	Hypergradient	$64^3$	.016	.016	4	4	$\infty$
Z754	Hypergradient	$64^3$	.020	.020	4	4	$\infty$
Z756	Hypergradient	$64^3$	.016	.016	4	4	1
Z757	Hypergradient	$64^3$	.016	.016	1	1	4

Table 7: Index of simulations. All simulations have  $\nu = \eta = 10^{-3}$ ,  $\nu_4 = \eta_4 = 2.5 \cdot 10^{-8}$ , and  $\Delta t = 0.003$ , except for Z677, which has  $\Delta t = 0.0012$ .  $I_{FFT} = \infty$  indicates that the FFT divergence correction is never applied. All finite-difference simulations utilize a radius-8 stencil and a phase-shift dealiasing correction.

### 5. Applications: Interpolation, refinement, and data analysis

The most accurate and most expensive interpolation procedure is direct evaluation of the Fourier series. Tuned finite differences provide a less expensive interpolation high-wavenumber interpolation. For example, in 2D, the centered interpolation (equation 4) provides function values halfway between grid points, and another interpolation along the diagonal yields the values at the grid centers. We have thus doubled the resolution of the grid, which we can do again if we wish. Note that we can do this for the entire grid or just for a subsection. After a few doublings, a simple linear interpolation serves to provide the function value at any point in space, yielding a 2D interpolation with the same wavenumber resolution as the component 1D interpolation. This procedure generalizes to arbitrary dimension.

As if it wasn't enough trouble to run large simulations on thousands of cpus, one is next confronted with analyzing large data cubes that are too big to fit in the memory of one machine.

Tuned operators allow for the construction of local local alternatives to global functions like the FFT. These include derivatives, dealiasing, filtering, and grid interpolation. Large output files can be stored in small easy-to-manage segments and operated on successively. For the purpose of data analysis, we have provided radius-16 tuned operators in table 3 that are accurate to 0.3 percent.

## 6. Acknowledgements

We thank Eric Blackman, Benjamin Chandran, Peggy Varniere, Yoram Lithwick, and Tim Dennis for useful discussions, and Yoram Lithwick for the FFT benchmark results. The simulations were run at the Pittsburgh Supercomputing Center’s Alpha ES45 “Lemieux” with the National Resource Allocation Committee grant MCA03S010P, and at the National Center for Supercomputing Applications’ Intel Itanium “Titan” with the grant AST020012N. The author was supported by Dr. Eric Blackman’s DOE grant DE-FG02-00ER54600 at the University of Rochester, and by Dr. Benjamin Chandran’s NSF grant AST-0098086 and DOE grants DE-FG02-01ER54658 and DE-FC02-01ER54651, at the University of Iowa.

## REFERENCES

Brandenburg, A., [lanl.arxiv.org/astro-ph/0109497](http://lanl.arxiv.org/astro-ph/0109497), 2001.

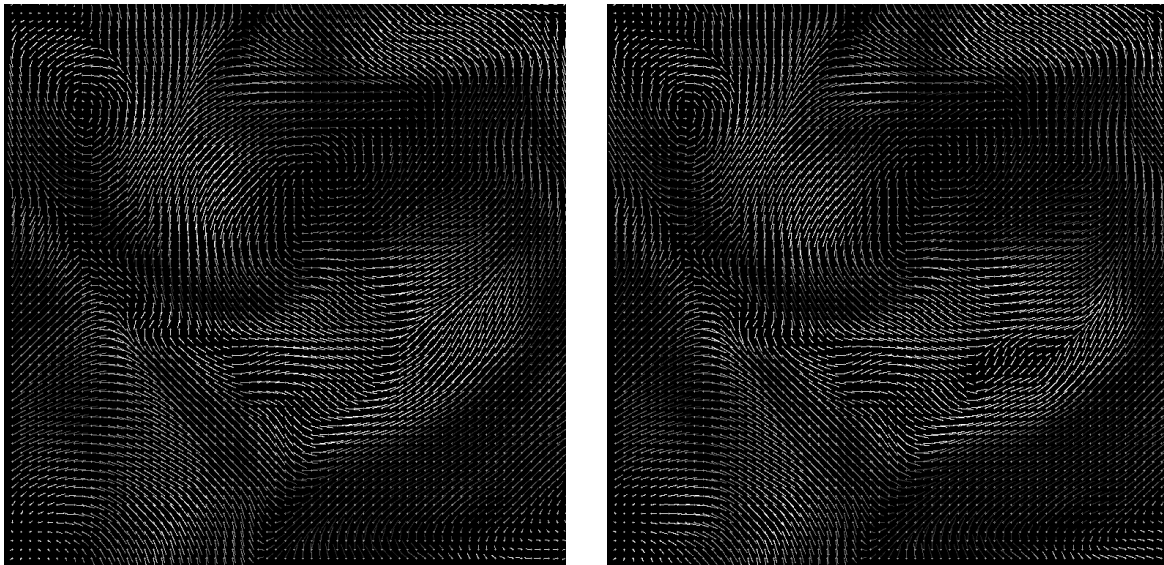


Fig. 4.— *Figure 4: The velocity field in a plane slice after  $t=.5$  for the tuned gradient simulation Z748 (left) and the spectral simulation Z677 (right). The arrow length gives the in-plane velocity and the arrow brightness indicates the component transverse to the plane.*

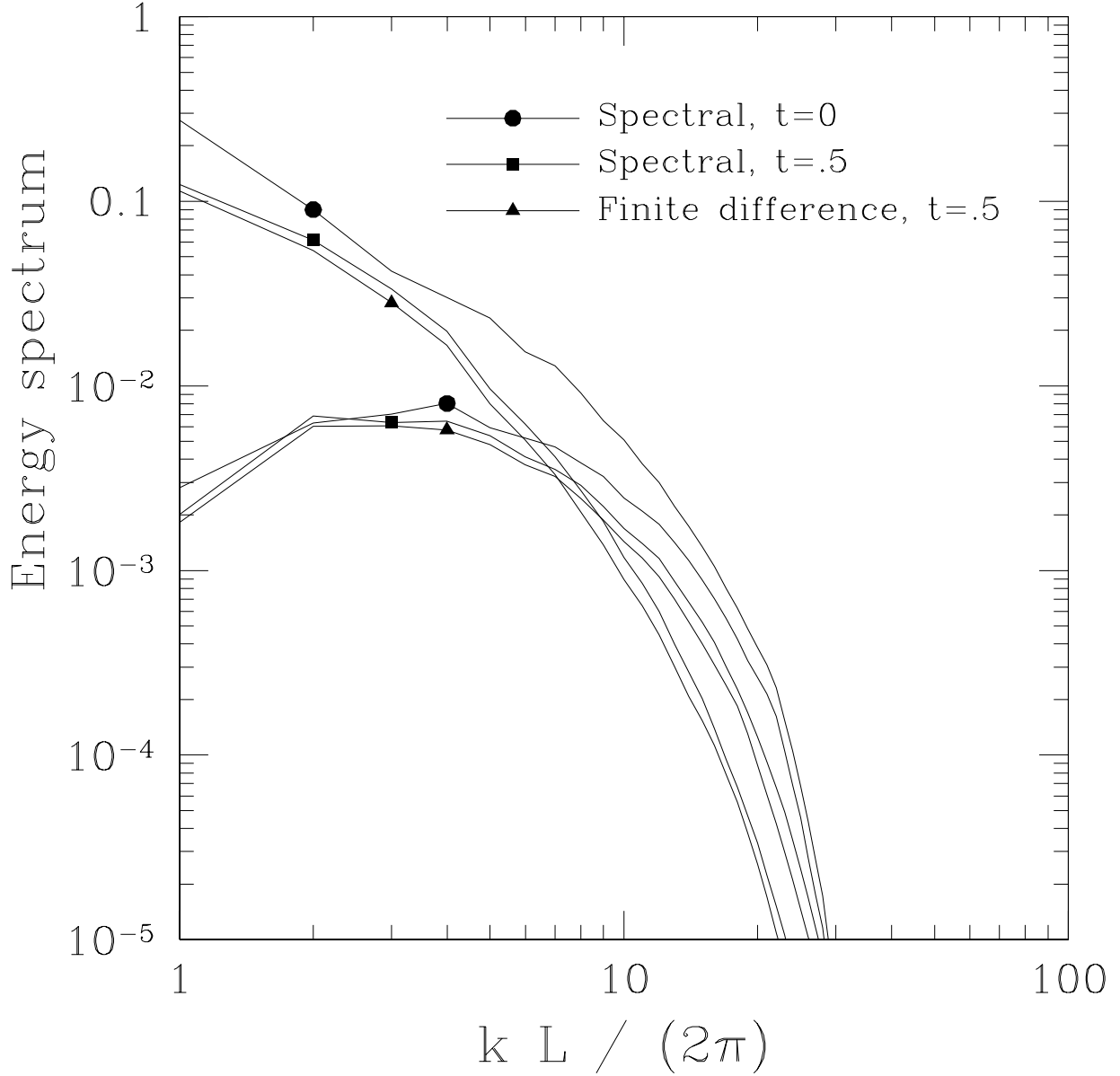


Fig. 5.— *Figure 5: The spectra for simulations Z748 and Z677, described in section 4.3.  $k$  is the wavenumber and  $L$  is the cube side length.*

Canuto, C., Hussaini, M. Y., Quarteroni, A., Zhang, t. A., “Spectral Methods in Fluid Dynamics”. Springer-Verlag 1987.

Dunigan, T., [www.csm.ornl.gov/~dunigan](http://www.csm.ornl.gov/~dunigan), 2004.

Frigo, M., & Johnson, S. G., 1998 ICASSP conference proceedings, vol. 3, pp. 1381-1384, “FFTW: An Adaptive Software Architecture for the FFT.”

Lele, S. K., J. Comp. Phys. 103, 16, 1992.

Maron, J., & Cowley, S., [lanl.arxiv.org/astro-ph/0111008](http://lanl.arxiv.org/astro-ph/0111008), 2001.

Maron, J. & Goldreich, P., ApJ, 554, 1175, 2001.

San Diego Supercomputing Center technical specifications, 2003,

[www.sdsc.edu/PMaC/Benchmark/maps\\_ping/maps\\_ping\\_results.html](http://www.sdsc.edu/PMaC/Benchmark/maps_ping/maps_ping_results.html)

Stone, J. & Norman, M., “Zeus-2D, A Radiation Magnetohydrodynamics Code for Astrophysical Flows in Two Space Dimensions: I. The Hydrodynamic Algorithms and Tests”, 1992a, ApJS, 80, 753.

Stone, J. & Norman, M., “Zeus-2D, A Radiation Magnetohydrodynamics Code for Astrophysical Flows in Two Space Dimensions: II. The Magnetohydrodynamic Algorithms and Tests”, 1992b, ApJS, 80, 791.